APL Materials

Surface stability of $SrNbO_{3+\delta}$ grown by hybrid molecular beam epitaxy

Cite as: APL Mater. **10**, 091112 (2022); https://doi.org/10.1063/5.0097699
Submitted: 30 April 2022 • Accepted: 29 August 2022 • Published Online: 22 September 2022

Suresh Thapa, Sydney R. Provence, Patrick T. Gemperline, et al.

Surface stability of $SrNbO_{3+\delta}$ grown by hybrid molecular beam epitaxy

Cite as: APL Mater. 10, 091112 (2022); doi: 10.1063/5.0097699
Submitted: 30 April 2022 • Accepted: 29 August 2022 •
Published Online: 22 September 2022

Suresh Thapa,[1] Sydney R. Provence,[1] Patrick T. Gemperline,[1] Bethany E. Matthews,[2] Steven R. Spurgeon,[2,3] Sydney L. Battles,[1] Steve M. Heald,[4] Marcelo A. Kuroda,[1] and Ryan B. Comes[1,a)]

AFFILIATIONS

[1] Department of Physics, Auburn University, Auburn, Alabama 36830, USA
[2] Energy and Environment Directorate, Pacific Northwest National Laboratory, Richland, Washington 99352, USA
[3] Department of Physics, University of Washington, Seattle, Washington 98195, USA
[4] Advanced Photon Source, Argonne National Laboratory, Argonne, Illinois 60439, USA

Note: This paper is part of the Special Topic on Materials Challenges and Synthesis Science of Emerging Quantum Materials.
[a)] **Author to whom correspondence should be addressed:** ryan.comes@auburn.edu

ABSTRACT

4d transition metal oxides have emerged as promising materials for numerous applications including high mobility electronics. $SrNbO_3$ is one such candidate material, serving as a good donor material in interfacial oxide systems and exhibiting high electron mobility in ultrathin films. However, its synthesis is challenging due to the metastable nature of the d^1 Nb^{4+} cation and the limitations in the delivery of refractory Nb. To date, films have been grown primarily by pulsed laser deposition (PLD), but development of a means to grow and stabilize the material via molecular beam epitaxy (MBE) would enable studies of interfacial phenomena and multilayer structures that may be challenging by PLD. To that end, $SrNbO_3$ thin films were grown using hybrid MBE for the first time using a tris(diethylamido)(tert-butylimido) niobium precursor for Nb and an elemental Sr source on $GdScO_3$ substrates. Varying thicknesses of insulating $SrHfO_3$ capping layers were deposited using a hafnium tert-butoxide precursor for Hf on top of $SrNbO_3$ films to preserve the metastable surface. Grown films were transferred *in vacuo* for x-ray photoelectron spectroscopy to quantify elemental composition, density of states at the Fermi energy, and Nb oxidation state. *Ex situ* studies by x-ray absorption near edge spectroscopy and scanning transmission electron microscopy illustrate that the $SrHfO_3$ capping plays an important role in preserving the crystalline quality of the material and the Nb $4d^1$ metastable charge state under atmospheric conditions.

INTRODUCTION

For two decades, the study of two-dimensional electron gas (2DEG) in complex metal oxides has rapidly increased after its observation at the $LaAlO_3$ (LAO)/$SrTiO_3$ (STO) interface.[1] This interesting phenomenon has driven ongoing research for two decades, opening the door for complex oxide interfaces as strong contenders for high carrier concentrations and high electron mobility. Oxide 2DEGs offer unique opportunities compared to traditional semiconductor ones as they may exhibit strong spin–orbit coupling along with the possibility of harnessing high carrier concentrations.[2,3] The search for a good donor oxide is a great challenge when building a high carrier concentration and mobility in oxide interface for high-speed electronics. Isoelectronic to the $SrVO_3$, $SrNbO_3$ (SNO) has a d^1 electronic configuration and a simple cubic perovskite structure with lattice parameter between 4.0 and 4.1 Å.[4] The band diagram of SNO reveals the Nb 4d t_{2g} bands crossing the Fermi level, indicating its metallic nature.[5] The low electron affinity of SNO makes it a promising interfacial donor material, as previously reported in density functional theory (DFT) studies on SNO/STO heterostructures.[6] Studies have also examined the material for use as a plasmonic transparent conducting material due to the large bandgap between the O 2p and Nb 4d bands.[7–9] Recent results have also suggested that epitaxial strain in SNO films can break cubic symmetry to produce a semimetallic tetragonal phase with extremely high mobility and an observed Berry phase, that make it promising for quantum material applications.[10] Large linear magnetoresistances of ~10^5 % and mobilities of 80 000 cm^2/V s

have also recently been reported in SNO/STO heterostructures,[11] suggesting that the material holds exceptional promise in topological and quantum material research.

Despite the great potential of SNO for interfacial charge transfer and topological phenomena, limited work has been carried out on synthesis of pristine SNO thin films. There are numerous unanswered questions on the basic properties of SNO, its surface stability, and its applications for interfacial engineering of emergent materials' properties. Previous reports on SNO thin film growth have employed pulsed laser deposition (PLD)[9–13] and sputtering.[7,8] There are no reports of MBE synthesis of SNO, though NbO_2[14] and Nb-doped STO[15] have been synthesized by MBE using an electron-beam evaporation source. In particular, previous work[12] examining the electronic band structure using *in situ* angle-resolved photoemission spectroscopy (ARPES) measurements provided insights into SNO thin films and verified the metallic character of SNO experimentally. However, this work also showed a significant excess of Nb^{5+} atomic valence relative to the expected 4+ charge state, which suppressed the spectral weight of electronic states near the Fermi level.[12] These results were attributed to surface Nb^{5+} states due to either Sr vacancies or formation of Nb_2O_5. However, adsorption of excess oxygen is also an alternative mechanism to accommodate the conversion from metastable Nb^{4+} to the stable d^0 Nb^{5+} state through the formation of a $Sr_2Nb_2O_7$ phase.[13,16,17] Similar results have also been observed previously in d^1 rare earth titanates[18,19] and $SrVO_3$[14,20]. Clearly, understanding and controlling the valence of Nb ions in SNO films is important to the development of interfacial heterostructures that leverage the d^1 electronic configuration and propensity of SNO to donate electrons to neighboring materials.[10,11]

One of the most promising approaches to preserve metastable SNO is by capping films with an alternative oxide with greater atmospheric stability. To date, there have been no reports of suitable capping layers for SNO. However, such an approach has been employed for $DyTiO_3$ films via a $LaAlO_3$ cap, which significantly enhanced the ratio of metastable Ti^{3+} vs d^0 Ti^{4+}[19] and in $SrVO_3$ with a TiO_x cap.[20] A perovskite oxide with a higher bandgap, matching A-site cation, and one that does not accept electrons from SNO would be a reasonable choice as a capping layer. $SrHfO_3$ (SHO) is well known for its large bandgap of 6.07 eV[21] and is expected to have a band alignment that prevents electron transfer,[5] which makes it an ideal perovskite oxide for capping in this system. However, the delivery of both Nb and Hf is highly challenging due to their refractory natures. To overcome this discrepancy, the hybrid molecular beam epitaxy technique opens opportunities for Nb and Hf to be supplied as metal organic precursors.

In addition to PLD, molecular beam epitaxy (MBE) is well established for the synthesis of various metal oxides over the last three decades. However, repeatable growth of a complex metal oxide incorporating refractory metal cations with stoichiometric control by traditional MBE is extra challenging as it lacks the adsorption-controlled growth window. In the past decade, hybrid MBE (hMBE) has been established as a state-of-the-art technique to grow complex metal oxides where refractory metals are supplied through a metal organic precursor and the A-site cation is supplied as a metallic source.[22] The hMBE technique is highly efficient in delivering low vapor pressure and refractory metals for repeatable growth of large varieties of high quality metal oxides such as $SrVO_3$,[23] $BaSnO_3$,[24] and $SrTiO_3$ (STO)[26,27] with improved stoichiometric control compared to the traditional MBE growth. Recent efforts in the synthesis of refractory metals such as Ir and Ru have also shown promise.[28,29] These approaches offer significant advantages over deposition with an electron-beam evaporator in an MBE, where achieving repeatable and stable growth conditions can be a challenge.

Selection of the precursor becomes highly important in perovskite oxide growth involving refractory metals as they determine the delivery of B-site cation. Previous reports[29,30] on synthesis of Nb_2O_5 by atomic layer deposition (ALD) suggest that niobium ethoxide (NbOEt) and tris(diethylamido)(tert-butylimido) niobium (TDTBN) are the most suitable Nb precursors. However, NbOEt decomposition, rather than evaporation in its molecular form, has been reported due to the significantly lower vapor pressure of NbOEt compared to TDTBN.[30] TDTBN is liquid at room temperature and was successfully evaporated for ALD at 65 °C using open boats due to the low vapor pressure of the precursor.[30] Recent work has shown both thermal and plasma-enhanced ALD of Nb_2O_5 using TDTBN.[31] In the case of thermal ALD, significant amounts of Nb^{4+} ions were observed in the films grown at high temperatures, likely because, unlike NbOEt, TDTBN contains no oxygen atoms in the molecule.[31] The chemical structure of the molecule is shown in Fig. 1. The lack of oxygen in the TDTBN precursor may afford greater control over the overall oxidation of the film because the delivery of molecular O_2 and oxygen plasma can be tuned to vary the oxygen chemical potential in the system over a wide range.

In this work, SNO band structure and partial density of states (pDOS) calculations are carried out by density functional theory (DFT). Metastable SNO films are grown on $GdScO_3$ substrates using hMBE. The surface of the film is monitored during growth by reflection high energy electron diffraction (RHEED), and *in vacuo* x-ray photoelectron spectroscopy (XPS) is used to check the stoichiometry of the film. Possible over-oxidation of the surface or of the film is studied by analyzing the Nb 3d core level on uncapped and SHO capped samples. Correlating the valence band features further allows the investigation of the effectiveness of SHO capping in preserving Nb^{4+} state. The surface roughness is analyzed using atomic force microscopy (AFM) topography. Further the Nb K-edge was analyzed using x-ray near-edge spectroscopy (XANES) to check the effect of SHO capping thickness on the Nb oxidation state.

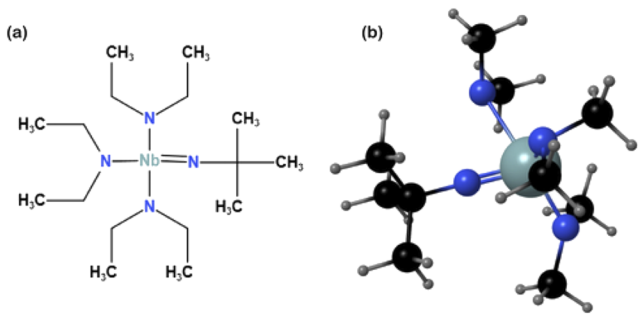

FIG. 1. (a) Structural formula and (b) ball and stick structure of tris (diethylamido)(tert-butylimido) niobium (TDTBN) precursor used for the hMBE growth of SNO epitaxial thin films.

METHODS

The electronic band structure of SNO was analyzed via DFT, using the Perdew–Burke–Ernzerhof (PBE) parameterization of the exchange–correlation energy.[32] No Hubbard U correction parameter was employed, consistent with previous models of the material.[10,12] Calculations employed projector-augmented-wave pseudopotentials[33] for the description of the atomic cores with cut-off energies of 40 and 400 Ry for the wave functions and density, respectively. Cubic unit cells were fully relaxed until forces were smaller than 1.36×10^{-7} eV/Å, and band structure calculations were performed. The self-consistent potential was determined using an $8 \times 8 \times 8$ Monkhorst–Pack mesh to sample the Brillouin zone. All calculations are carried out using the Quantum Espresso software.[34]

Uncapped and SHO capped SNO thin films of identical thickness were grown on (110) $GdScO_3$ (GSO, pseudocubic lattice parameter 3.96 Å; lattice mismatch = −1.5%) single crystal substrates (MTI Crystal) in a Mantis MBE reactor with a baseline pressure of $\sim 10^{-9}$ Torr. Additional samples were grown on (001) $SrTiO_3$ (STO, 3.905 Å) substrates that exhibit significantly larger lattice mismatch (−2.9%) and are reported for completeness in the supplementary material. These films exhibited island growth and rougher surfaces, similar to what has been reported previously for films grown by pulsed laser deposition.[13] All the substrates were ultrasonically cleaned in acetone and isopropanol and dried with dry nitrogen gas. All the substrates were cleaned in oxygen in the MBE growth chamber by ramping to the 1000 °C growth temperature over ∼1 h as measured by a thermocouple.[25,35] We estimate that the setpoint was ∼150–200 °C higher than substrate surface temperature due to the absence of backside substrate metallization, resulting in GSO surface temperature between 800 and 850 °C. Cleaning and SNO (SHO) growths were performed in a background pressure of $\sim 3 \times 10^{-6}$ Torr and $\sim 3.6 \times 10^{-6}$ ($\sim 1 \times 10^{-5}$) Torr O_2, respectively. Calibration samples showed that the absorption of B-site cations takes a longer time compared to the low flux of A-site cation. To control the exposure duration, alternate shutter deposition is applied to supply A- and B-site cations in both SNO and SHO deposition. For the metalorganic sources, a pneumatic ALD valve (Swagelok 316L) is used to isolate the sources when they are not depositing and serves as the shutter for the deposition.

A series of uncapped and SHO-capped SNO samples were grown where Sr and tris(diethylamido)(tert-butylimido) niobium (TDTBN) fluxes were held fixed. The flux of SrO is measured by quartz crystal microbalance (QCM) in Å/s. Strontium (99.99%, Sigma-Aldrich, USA) was supplied through a low temperature effusion cell. The Sr flux was calibrated using QCM under oxygen environment with measured chamber pressure of 3×10^{-6} Torr. Niobium was supplied through a gas source using the TDTBN metal–organic precursor (99.99%, Sigma-Aldrich, USA) from a bubbler connected to the growth chamber using the ALD pneumatic valve and a heated gas injector source (E-Science, USA). No carrier gas was used. The gas injector was held at 90 °C using a proportional–integral–differential (PID) controller and the bubbler at 73 °C through external heating tape and a PID controller. While the vapor pressure was not measured directly, the chamber pressure showed only marginal changes (∼1%) upon valve actuation, suggesting that the vapor pressure is in the range 1–100 mTorr that is commonly employed for hMBE using a pressure-control feedback system.[22] This configuration can thus be thought of as a modified metal–organic evaporation source that replicates the capabilities of a low temperature effusion cell for organic molecules.

The growth chamber shroud walls were maintained at −30 °C via a closed loop chiller and low temperature fluid (Syltherm XLT, Dow Chemical) to reduce the background water vapor pressure from the dissociated TDTBN molecules. The chamber pressure measured by the cold cathode gauge generally increases and reaches one unit higher at 10^{-6} Torr for the first 5–10 s as the TDTBN supply valve is opened before stabilizing due to the dissociated and unreacted TDTBN injected into the system. O_2 flow is turned off for the uncapped sample during cooldown to minimize over-oxidation of the film or of the surface of the film. Right after the SNO deposition, the hafnium tert-butoxide (HTB) flux is calibrated, and varying thickness of SHO capping layers were deposited, turning on O_2 flow with measured chamber pressure of $\sim 1 \times 10^{-5}$ Torr O_2. Hafnium was supplied through a gas source using a metalorganic precursor, HTB (99.999%, Sigma-Aldrich, USA) from a bubbler connected to the growth chamber without carrier gas and controlled using a traditional pressure-control feedback loop.[22,36] Here, we present four representative samples among all the samples, including one uncapped and three capped, annotated as thin (2 unit cells, ∼0.8 nm), medium (3 unit cells, ∼1.2 nm), and thick (4 unit cells, ∼1.6 nm) capped.

In situ RHEED (Staib Instruments) was used to monitor the growth process and the quality of the films. Analysis of RHEED videos was performed using principal component analysis and *K*-means clustering software that has been described previously.[37] After growth, the samples were transferred from the MBE reactor to the PHI 5400 x-ray photoelectron spectroscopy (XPS) (Al Kα x-ray source) system through an ultra-high vacuum (UHV) transfer line.[38] An electron neutralizer gun was applied to compensate charging of the insulating samples. The surface stoichiometry of all grown samples was characterized by analyzing the core level and correlated with the valence band XPS spectra measured with base pressure of $\sim 1 \times 10^{-9}$ Torr. Analysis of the XPS data was performed using CasaXPS.[39] The Sr:Nb cation stoichiometry was determined to be an ideal one-to-one ratio with ∼5% uncertainty for calibration films and uncapped samples using sensitivity factors for the Sr 3d and Nb 3d peaks. Due to the close overlap of Sr and Nb in the atomic mass, other techniques such as Rutherford back scattering were not practical for stoichiometry determination. To properly align all core level peaks, the valence band is fitted with a Fermi–Dirac function, and all peaks are shifted with respect to the Fermi level because the charge neutralizer prevents the direct determination of the Fermi level. A representative fit is shown in Fig. S8 in the supplementary material. A Rigaku Smartlab XRD equipped with a four-circle goniometer and a Cu $K\alpha_1$ radiation line isolated with a double bounce Ge (220) monochromator was used for 2θ-ω scans on the (002) reflection of the SNO samples. X-ray absorption near-edge spectroscopy (XANES) was performed at the Advanced Photon Source at Sector 20-BM in fluorescence mode for both in-plane (parallel) and out-of-plane (perpendicular) polarized x rays at the Nb K edges. Cross-sectional scanning transmission electron microscopy (STEM) samples were prepared using a Thermo Fisher Helios G4 Hydra Plasma Focused Ion Beam (PFIB) microscope with a standard lift out procedure using Xe+ ions. Final 5 kV thinning and 2 kV

polish were performed using Ar+ ions. STEM images were acquired on a probe-corrected Thermo Fisher Themis Z microscope operating at 300 kV, with a convergence semi-angle of 25.2 mrad and an approximate collection angle range of 65–200 mrad for high-angle annular dark field (STEM-HAADF) images. STEM energy-dispersive x-ray spectroscopy (STEM-EDS) composition maps were acquired using a SuperX detector.

RESULTS

Figure 2(a) shows the cubic crystal structure of perovskite SNO where a niobium cation is octahedrally coordinated by oxygen ions. A lattice parameter of 4.02 Å was obtained using DFT calculations, which is in agreement with previous work.[4] The band structure and corresponding density of states (DOS) that provide context to interpret experimental results of SNO are shown in Fig. 2(b). The metallic nature of SNO is observed with the Fermi level crossing conduction bands primarily formed by Nb 4d states, consistent with its d^1 electronic configuration. The O 2p bands make significant contributions to the band structure of SNO in the vicinity of the Fermi level. Fully occupied valence bands are composed mainly by the O 2p. The gap between the O 2p and Nb 4d bands is ~2.4 eV. These results agree with previous DFT reports.[12]

To test the efficacy of TDTBN as a precursor, SNO thin films were grown on GSO substrates by hMBE. Figures 3(a) and 3(b) shows the RHEED images for uncapped SNO films grown on GSO

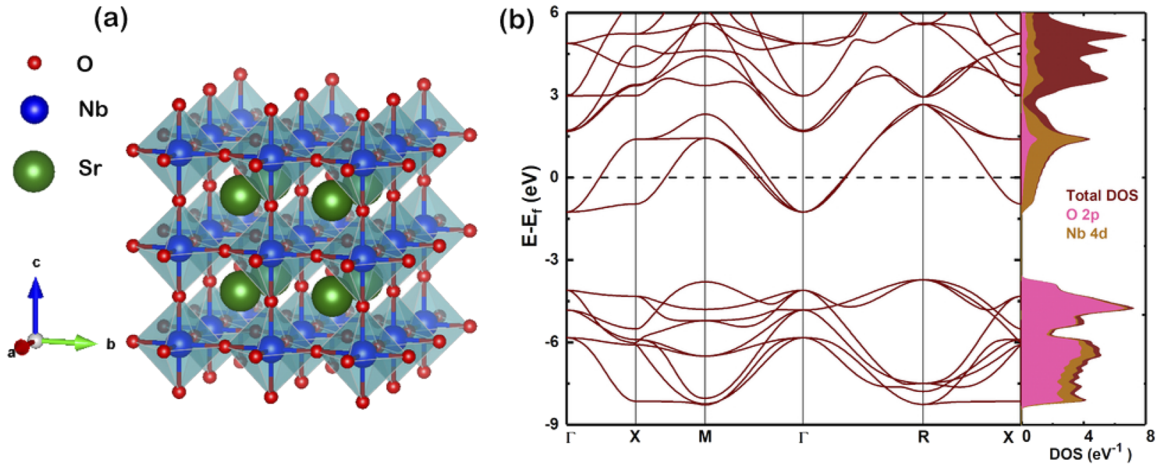

FIG. 2. (a) Cubic perovskite structure of $SrNbO_3$, (b) band dispersion and density of states (DOS) of $SrNbO_3$. Orbital decomposition onto localized atomic orbitals from Nb 4d and O 2p is shown in gold and pink, respectively.

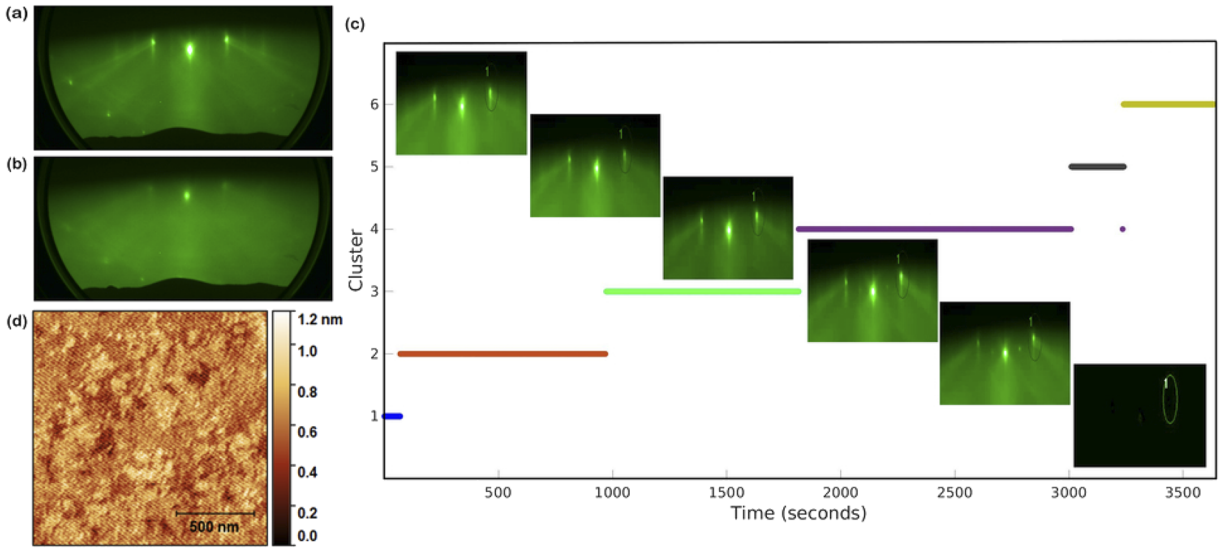

FIG. 3. RHEED image of SNO film (a) hot right after growth and (b) after cooling down on GSO along 110 azimuth, (c) *K*-means clustering (d) AFM topography of uncapped SNO films, (d) XRD on uncapped and SHO capped samples.

along the [110] azimuth immediately after growth at high temperature and after the sample is cooled down to room temperature. Intense diffraction spots as well as sharp Kikuchi bands in Fig. 3(a) indicate that the sample is smooth, with a well-crystallized surface film. However, the diffraction spots along with Kikuchi bands lose their intensity after the sample is cooled as shown in Fig. 3(b), indicating degradation in surface crystal quality. Figure 3(c) shows the *K*-means clustering analysis of the film growth, showing the gradual evolution of the film during the hour-long growth process.[37] Clusters indicate a centroid image that minimizes the error from all images acquired in the video over the course of the growth. The initial surface reconstruction from the GSO substrate terminates after ~1 nm of growth and the surface evolves slowly with few changes to the pattern for the remainder of the growth. The total film thickness is ~3 nm due to the low vapor pressure of the TDTBN precursor and the slow kinetics required to obtain good oxygen stoichiometry in the material during growth. Similar growth kinetics has been reported for metastable $NdTiO_3$ films grown by hybrid MBE.[40] Thicker films showed gradual decay in the quality of the RHEED pattern, likely due to strain relaxation and accumulation of excess oxygen during the growth. This has also been observed in the $NdTiO_3$ films as they reach ~5 nm in thickness.[40] Future work will explore increasing growth rates at different evaporation temperatures, though the slow growth rate is not a significant barrier to interfacial studies of charge transfer.

One possible explanation for the degraded surface quality after cooldown is the over-oxidation of the film surface due to the presence of residual oxygen and water in the chamber, which cannot be pumped out quickly enough after the growth. Water is also a likely by-product of the decomposition of the precursor, raising the partial pressure in the chamber during and after the growth process. A second possible reason may be due to adsorbed nitrogen and carbon on the film surface as a by-product from metal organics as shown in XPS spectra for the uncapped sample in supplementary material S1.

To further explore the role of surface oxidation after the growth process, a series of samples were grown with an SHO capping layer deposited immediately after the conclusion of the SNO growth. The SNO samples show consistently improved RHEED images after capping with SHO and cooling to room temperature, which can be found in the supplementary material in Fig. S2. Diffracted peaks remain sharper than what are shown in Fig. 3(b). This indicates high crystallinity of the SHO capping layer and better preservation of SNO from over-oxidation during cooldown. It should be noted that the medium-capped SNO sample shows relatively weak RHEED pattern after SHO capping as found in Fig. S2 because of inconsistent Hf flux that produced a Hf-rich capping layer.

AFM measurements were performed to verify the surface morphology of the SNO films. Figure 3(d) shows the AFM topography of an uncapped SNO film grown on a GSO substrate with surface roughness of 1.0 Å, indicating that the film is highly smooth. Additionally, AFM topography of SHO shows a surface roughness of 1.4 Å, as illustrated in supplementary material Fig. S3, indicating a smooth capping surface. XRD data are shown in the supplementary material Fig. S4 for uncapped and SHO capped SNO films grown on GSO substrates. An uncapped SNO sample exhibits no peak, likely due to full amorphization after air exposure. Meanwhile capped samples have peaks consistent with the convolution of an extremely thin SHO/SNO bilayer. Fits to the data have significant uncertainty due to the convolution of the peaks, but are consistent with a lattice constant for SNO of 4.07 Å and SHO of 4.18 Å. The SNO value is close to the previous report by Bigi *et al.* on GSO substrates of 4.09 Å.[12] Meanwhile the SHO lattice constant is consistent with what would be expected for a coherently strained SHO film (a_{bulk} = 4.11 Å[41]) that is under out-of-plane tensile strain due to mismatch with the GSO substrate. The intensity of an extra peak increases with increasing thickness of a capping, reflecting improved stoichiometry and crystallinity, as predicted by RHEED.[42]

To probe the role of capping on preservation of the Nb^{4+} state, *in situ* XPS analysis of the Nb 3d core level on uncapped and SHO capped SNO films was performed. Figures 4(a)–4(d) show the Nb 3d core level deconvolution for uncapped and SHO capped SNO films using constraints from Table S1 as provided in the supplementary material. As the Hf 4d core level significantly overlaps with the Nb 3d core level, the peaks must be carefully deconvoluted to determine the ratio of Nb^{4+} to Nb^{5+}. The area ratio $A_{Nb^{4+}}/(A_{Nb^{4+}} + A_{Nb^{5+}})$is shown in the inset to Fig. 4(e), with the value increasing from 28% for the uncapped sample to 37% for the 1.6 nm capped sample. A clear extra peak at lower binding energy in Nb 3d is significantly increased in capped samples compared to an uncapped sample that reflects that the SHO capping is highly effective in preserving the Nb^{4+} state. This peak has previously been observed after sputter cleaning of NbO_2 after atmospheric exposure[42] and *in situ* for high-quality NbO_2 films grown by MBE using an electron-beam evaporation source.[14] *In situ* measurements of uncapped $SrNbO_3$ films grown by PLD showed significantly smaller concentrations of Nb^{4+} by comparison,[12] indicating that the $SrHfO_3$ capping layer is important even for *in situ* studies of the material. It is important to note that if one assumes an abrupt interface between SHO and SNO, the SHO capping layer should have no impact on the peak area ratios between Nb^{4+} and Nb^{5+}. Furthermore, if any Nb were to diffuse out into the SHO cap or to the film surface, it would be more likely to oxidize to the 5+ charge state, which would result in underestimating the amount of Nb^{4+} in the bulk of the film, thanks to the surface sensitivity of XPS measurements.[38] However, it is clear that some Nb^{5+} is still present even in the capped samples, leading to a chemical formula of $SrNbO_{3+\delta}$ for the material.

XPS valence band spectra were acquired simultaneously with the Nb 3d core level data to measure the density of states for the Nb 4d electronic states near the Fermi level. Figure 4(e) shows the valence band spectra for uncapped and SHO capped samples. The thickness and quality of the capping layer plays a clear role in the preservation of the single Nb 4d electron at the Fermi level, with the thickest capping layer providing the largest peak. The medium-capped sample shows relatively lower electron concentration compared to a thin capped sample as shown in Fig. 4(e). That is likely related to the off-stoichiometry of the SHO capping layer, governed by the fluctuation in the Hf flux during SHO deposition for that sample. This can be inferred from Fig. 3(b) as we see a more intense Hf 4d core level compared to Nb 3d core level among all capped samples. This result can also be correlated with the lowest quality RHEED image for a medium capped film as shown in middle panel of Fig. S1. It is thus clear that the effectiveness of SHO as a capping layer for SNO is dependent on the crystalline quality of the SHO film.

XANES offers a more bulk-sensitive probe of the Nb valence after atmospheric exposure. Hence, to supplement the XPS

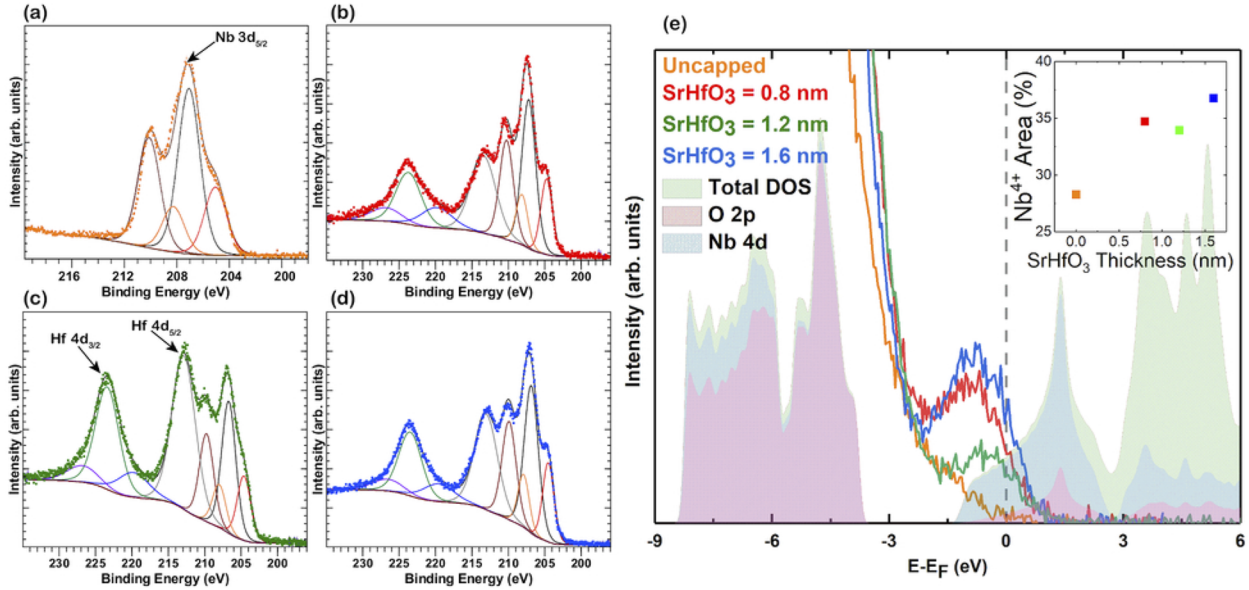

FIG. 4. Nb 3d core level deconvolution for SNO thin films capped with (a) uncapped, (b) thin (0.8 nm) capped, (c) medium (1.2 nm) capped, and (d) thick (1.6 nm) capping of SHO. Fits to the data show spin–orbit split peaks of Nb^{4+} (low binding energy) and Nb^{5+} (high binding energy) features. (e) Valence band XPS data showing density of states near the Fermi level for all four samples. Partially transparent density of states from DFT model of $SrNbO_3$ is taken from Fig. 2.

analysis on oxidation state of Nb in the film, XANES analysis on Nb *K*-edge was also carried out. Figure 5 shows the XANES spectra on the Nb K-edge for SHO-capped samples with reference spectra for Nb^{4+} (NbO_2) and Nb^{5+} (Nb_2O_5).[43] The inset of the figure shows a narrower region to resolve the data for the three samples. The

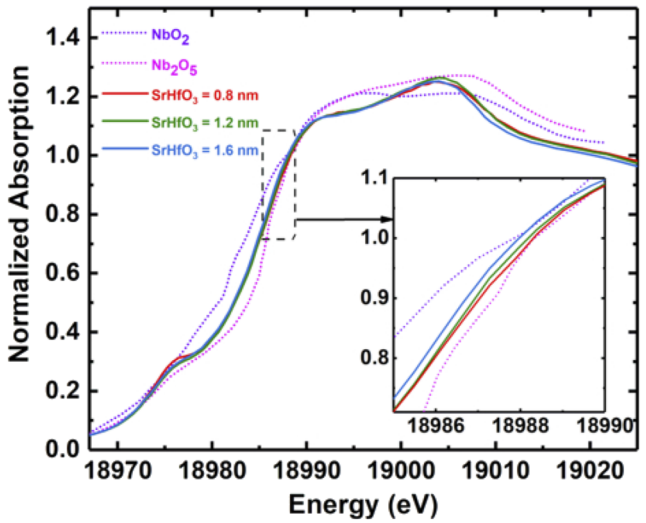

FIG. 5. Nb *K* edge XANES data for three $SrHfO_3$-capped samples. NbO_2 (Nb^{4+}) and Nb_2O_5 (Nb^{5+}) reference spectra were taken from Marini *et al.*[43] (Inset) High-resolution perspective of three capped samples showing enhanced Nb^{4+} charge state in the sample with 1.6 nm capping layer.

Nb *K*-edge shows that the pre-edge features of the 0.8 and 1.2 nm samples mirror Nb_2O_5 spectra, indicating more Nb^{5+} state compared to the 1.6 nm sample. The white line is also shifted to greater photon energy for the 0.8 and 1.2 nm samples, consistent with a higher formal charge. Differences between 0.8 and 1.2 nm are quite small and likely within the uncertainty of the measurement. In the thickest capped sample, the spectrum white line is shifted to lower photon energy, indicating the greatest concentration of Nb^{4+} state among all of the samples. This observation indicates that the capping has great role in preserving the Nb oxidation state in SNO films after air exposure. We suggest that at least 4 unit cells of an insulator such as SHO are needed to provide a good oxidation barrier in air.

To further characterize the role of the SHO capping layer in preserving the crystalline quality of ultrathin SNO films, a 2 unit-cell SNO film with a 3 unit-cell SHO cap was measured via scanning transmission electron microscopy (STEM). Figure 6(a) shows a wide-field STEM high-angle annular dark-field (STEM-HAADF) image, demonstrating the uniform interfaces throughout the sample, while Figs. 6(b)–6(d) show a drift-corrected set of high-resolution STEM-HAADF and STEM bright-field (STEM-BF) images. The atomic-resolution images show that the crystalline SNO layer is preserved by the SHO cap and that intermixing is minimal. The SNO layer in the *Z*-contrast STEM-HAADF image is darker due to the lower atomic number (*Z*) of Nb compared to Hf and Gd. An atomic-resolution STEM energy-dispersive x-ray spectroscopy (STEM-EDS) map was also acquired, which is shown in the supplementary material. Due to the close overlap of various Sr, Hf, and Nb x-ray edges, it is difficult to resolve clear interfaces, but the interface between GSO and SNO shows minimal intermixing over ~1 unit cell.

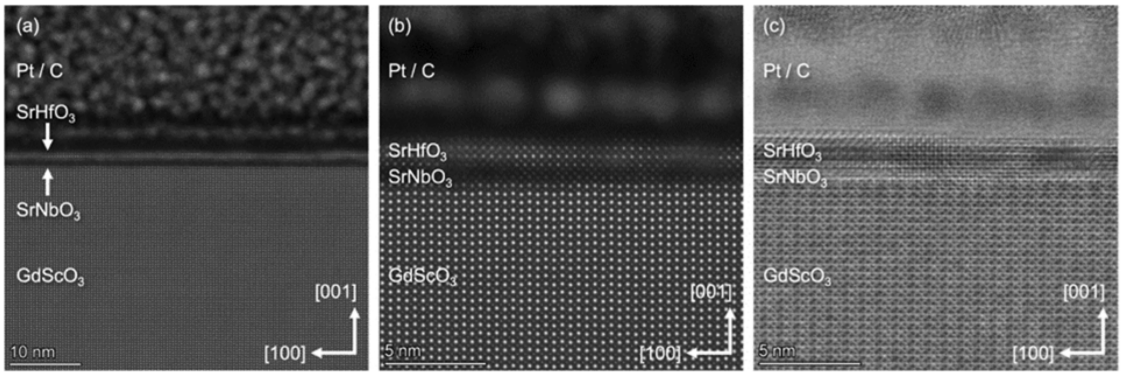

FIG. 6. Cross-sectional scanning transmission electron microscopy (STEM) images of $SrHfO_3/SrNbO_3/GdScO_3$ heterostructure. (a) Wide-field STEM high-angle annular dark-field (STEM-HAADF), (b) high-resolution STEM-HAADF, and (c) STEM bright-field (STEM-BF) images, respectively.

DISCUSSION AND CONCLUSION

Successful growth of metastable SNO by hMBE using the TDTBN precursor has been demonstrated for the first time. The good lattice match to the GSO substrate supported the growth of high quality epitaxial SNO films, which can be inferred from the high quality RHEED images in Figs. 3(a) and S1. Degrading the RHEED quality of an uncapped sample during cooldown shows that the SNO film surface over-oxidizes during cooldown, which may be attributed to residual oxygen, water vapor from the decomposed metal–organic precursor, or scavenging of other radicals in the system. Our observation shows that minimizing exposure to reactive gases after film growth is critical to preserving a stable film surface, as shown in the RHEED images in the supplemental information and the valence band density of states in Fig. 4. Over-oxidation of the SNO film surface can be reduced by depositing a dielectric capping layer such as SHO. Cooling in vacuum for uncapped samples reduces the formation of competing phases such as amorphous $Sr_2Nb_2O_7$.[13] However, surface-sensitive studies such as XPS and ARPES are still likely to detect the majority of the signal from the top few unit cells where Nb^{5+} will be the dominant charge state. On the other hand, *ex situ* AFM topography reveals that uncapped samples are highly smooth even after air exposure, suggesting that amorphization due to adsorption of oxygen or other radicals is fairly uniform across the sample. This indicates that a smooth surface is not sufficient evidence to confirm ideal oxygen stoichiometry at the film surface. Thus, we suggest that future studies on ultrathin SNO films should take care to decouple intrinsic phenomena related to the novel physics that can occur in the system, from features that may occur due to variation in oxygen stoichiometry away from the ideal $SrNbO_3$ chemical formula. Transport measurements on these samples would require great care to determine the fundamental properties of SNO and may benefit from complementary measurements such as terahertz spectroscopy in SNO samples buried under capping layers. Previous studies of SNO as a quantum material have not used this approach,[4,10,12] and we suggest that further exploration of buried SNO layers may be warranted.

In conclusion, our study of the synthesis of metastable $SrNbO_{3+\delta}$ thin films demonstrates the capabilities of the hMBE technique with a new TDTBN precursor. As predicted by our DFT calculations, the SNO films have valence band features at the Fermi level, based on XPS analysis, which is strongly dependent on the Nb charge state. The surface of the sample is preserved during cooldown by depositing a capping layer of $SrHfO_3$ immediately after $SrNbO_3$ growth, which increases the electronic density of states near the Fermi level. XRD, STEM, XAS, and XPS used to characterize the SNO film and effectiveness of the SHO capping at various thicknesses indicate that both the quality and the thickness of the capping layer are important to preserving the surface. However, we have shown that high-quality SHO capping layers can preserve the crystalline quality of even ultrathin SNO layers as thin as 2 unit cells. The ability to deposit $SrNbO_3$ films by hMBE opens the door for future exploration of interfacial phenomena in heterostructures, where it is expected to be a powerful electron donor in 2D systems.

SUPPLEMENTARY MATERIAL

See the supplementary material for additional figures, including atomic force microscopy, x-ray diffraction, RHEED, STEM-EDS, and x-ray photoelectron spectroscopy.

ACKNOWLEDGMENTS

S.T., S.R.P., and R.B.C. acknowledge support from the Air Force Office of Scientific Research for the film synthesis and characterization under Award No. FA9550-20-1-0034. P.T.G. and S.L.B. gratefully acknowledge support for RHEED analytics from the National Science Foundation (NSF) under Award No. DMR-2045993. XRD measurements were performed using an instrument acquired through the NSF Major Research Instrumentation Program under Award No. DMR-2018794. B.E.M. and S.R.S. were supported by the Chemical Dynamics Initiative/Investment, under the Laboratory Directed Research and Development (LDRD) Program at Pacific Northwest National Laboratory (PNNL). PNNL is a multi-program national laboratory operated for the U.S. Department of Energy (DOE) by Battelle Memorial Institute under Contract No. DE-AC05-76RL01830. This research used resources of the

Advanced Photon Source, an Office of Science user facility operated for the U.S. Department of Energy (DOE) Office of Science by Argonne National Laboratory, and was supported by the U.S. DOE under Contract No. DE-AC02-06CH11357.

AUTHOR DECLARATIONS

Conflict of Interest

The authors have no conflicts to disclose.

Author Contributions

Suresh Thapa: Investigation (lead); Visualization (lead); Writing – original draft (lead); Writing – review & editing (equal). **Sydney R. Provence**: Investigation (equal). **Patrick T. Gemperline**: Investigation (equal); Visualization (equal). **Bethany E. Matthews**: Formal analysis (supporting); Investigation (supporting); Writing – review & editing (supporting). **Steven R. Spurgeon**: Formal analysis (supporting); Investigation (supporting); Writing – review & editing (supporting). **Sydney L. Battles**: Investigation (supporting); Visualization (supporting). **Steve M. Heald**: Investigation (supporting). **Marcelo A. Kuroda**: Formal analysis (supporting); Investigation (supporting); Supervision (supporting); Writing – review & editing (supporting). **Ryan B. Comes**: Conceptualization (equal); Funding acquisition (equal); Investigation (equal); Supervision (equal); Writing – original draft (equal); Writing – review & editing (equal).

DATA AVAILABILITY

The data that support the findings of this study are available from the corresponding author upon reasonable request.

REFERENCES

[1] A. Ohtomo and H. Y. Hwang, Nature **427**, 423 (2004).
[2] Y. Chen and R. J. Green, Adv. Mater. Interfaces **6**, 1900547 (2019).
[3] J. Mannhart, D. H. A. Blank, H. Y. Hwang, A. J. Millis, and J.-M. Triscone, MRS Bull. **33**, 1027 (2008).
[4] D. Oka, Y. Hirose, S. Nakao, T. Fukumura, and T. Hasegawa, Phys. Rev. B **92**, 205102 (2015).
[5] Z. Zhong and P. Hansmann, Phys. Rev. X **7**, 011023 (2017).
[6] Z. Zhong and P. Hansmann, Phys. Rev. B **93**, 235116 (2016).
[7] J. Roth, A. Paul, N. Goldner, A. Pogrebnyakov, K. Agueda, T. Birol, N. Alem, and R. Engel-Herbert, ACS Appl. Mater. Interfaces **12**, 30520 (2020).
[8] Y. Park, J. Roth, D. Oka, Y. Hirose, T. Hasegawa, A. Paul, A. Pogrebnyakov, V. Gopalan, T. Birol, and R. Engel-Herbert, Commun. Phys. **3**, 102 (2020).
[9] M. Mirjolet, M. Kataja, T. K. Hakala, P. Komissinskiy, L. Alff, G. Herranz, and J. Fontcuberta, Adv. Opt. Mater. **9**, 2100520 (2021).
[10] J. M. Ok, N. Mohanta, J. Zhang, S. Yoon, S. Okamoto, E. S. Choi, H. Zhou, M. Briggeman, P. Irvin, A. R. Lupini, Y.-Y. Pai, E. Skoropata, C. Sohn, H. Li, H. Miao, B. Lawrie, W. S. Choi, G. Eres, J. Levy, and H. N. Lee, Sci. Adv. **7**, eabf9631 (2021).
[11] J. Zhang, J. M. Ok, Y.-Y. Pai, J. Lapano, E. Skoropata, A. R. Mazza, H. Li, A. Huon, S. Yoon, B. Lawrie, M. Brahlek, T. Z. Ward, G. Eres, H. Miao, and H. N. Lee, Phys. Rev. B **104**, L161404 (2021).
[12] C. Bigi, P. Orgiani, J. Sławińska, J. Fujii, J. T. Irvine, S. Picozzi, G. Panaccione, I. Vobornik, G. Rossi, D. Payne, and F. Borgatti, Phys. Rev. Mater. **4**, 025006 (2020).
[13] K. R. Balasubramaniam, Y. Cao, N. Patel, S. Havelia, P. J. Cox, E. C. Devlin, E. P. Yu, B. J. Close, P. M. Woodward, and P. A. Salvador, J. Solid State Chem. **181**, 705 (2008).
[14] C. Lin, A. Posadas, T. Hadamek, and A. A. Demkov, Phys. Rev. B **92**, 035110 (2015).
[15] Z. H. Lim, N. F. Quackenbush, A. N. Penn, M. Chrysler, M. Bowden, Z. Zhu, J. M. Ablett, T.-L. Lee, J. M. LeBeau, J. C. Woicik, P. V. Sushko, S. A. Chambers, and J. H. Ngai, Phys. Rev. Lett. **123**, 026805 (2019).
[16] C. Chen, Z. Wang, F. Lichtenberg, Y. Ikuhara, and J. G. Bednorz, Nano Lett. **15**, 6469 (2015).
[17] C. Chen, S. Lv, Z. Wang, K. Akagi, F. Lichtenberg, Y. Ikuhara, and J. G. Bednorz, Appl. Phys. Lett. **105**, 221602 (2014).
[18] P. Xu, Y. Ayino, C. Cheng, V. S. Pribiag, R. B. Comes, P. V. Sushko, S. A. Chambers, and B. Jalan, Phys. Rev. Lett. **117**, 106803 (2016).
[19] R. Aeschlimann, D. Preziosi, P. Scheiderer, M. Sing, S. Valencia, J. Santamaria, C. Luo, H. Ryll, F. Radu, R. Claessen, C. Piamonteze, and M. Bibes, Adv. Mater. **30**, 1707489 (2018).
[20] S. Caspi, L. Shoham, M. Baskin, K. Weinfeld, C. Piamonteze, K. A. Stoerzinger, and L. Kornblum, J. Vac. Sci. Technol. A **40**, 013208 (2022).
[21] C. Rossel, M. Sousa, C. Marchiori, J. Fompeyrine, D. Webb, D. Caimi, B. Mereu, A. Ispas, J. P. Locquet, H. Siegwart, R. Germann, A. Tapponnier, and K. Babich, Microelectron. Eng. **84**, 1869 (2007).
[22] M. Brahlek, A. S. Gupta, J. Lapano, J. Roth, H. T. Zhang, L. Zhang, R. Haislmaier, and R. Engel-Herbert, Adv. Funct. Mater. **28**, 1702772 (2018).
[23] C. Eaton, J. A. Moyer, H. M. Alipour, E. D. Grimley, M. Brahlek, J. M. LeBeau, and R. Engel-Herbert, J. Vac. Sci. Technol. A **33**, 061504 (2015).
[24] A. Prakash, T. Wang, R. Choudhary, G. Haugstad, W. L. Gladfelter, and B. Jalan, J. Vac. Sci. Technol. A **38**, 063410 (2020).
[25] B. Jalan, R. Engel-Herbert, N. J. Wright, and S. Stemmer, J. Vac. Sci. Technol. A **27**, 461 (2009).
[26] S. Thapa, S. R. Provence, D. Jessup, J. Lapano, M. Brahlek, J. T. Sadowski, P. Reinke, W. Jin, and R. B. Comes, J. Vac. Sci. Technol. A **39**, 053203 (2021).
[27] W. Nunn, A. K. Manjeshwar, J. Yue, A. Rajapitamahuni, T. K. Truttmann, and B. Jalan, Proc. Natl. Acad. Sci. U. S. A. **118**, e2105713118 (2021).
[28] W. Nunn, S. Nair, H. Yun, A. Kamath Manjeshwar, A. Rajapitamahuni, D. Lee, K. A. Mkhoyan, and B. Jalan, APL Mater. **9**, 091112 (2021).
[29] K. Kukli, M. Ritala, M. Leskelä, and R. Lappalainen, Chem. Vap. Depos. **04**, 29 (1998).
[30] T. Blanquart, J. Niinistö, M. Heikkilä, T. Sajavaara, K. Kukli, E. Puukilainen, C. Xu, W. Hunks, M. Ritala, and M. Leskelä, Chem. Mater. **24**, 975 (2012).
[31] S. B. Basuvalingam, B. Macco, H. C. M. Knoops, J. Melskens, W. M. M. Kessels, and A. A. Bol, J. Vac. Sci. Technol. A **36**, 041503 (2018).
[32] J. P. Perdew, K. Burke, and M. Ernzerhof, Phys. Rev. Lett. **77**, 3865 (1996).
[33] P. E. Blöchl, Phys. Rev. B **50**, 17953 (1994).
[34] P. Giannozzi, O. Andreussi, T. Brumme, O. Bunau, M. Buongiorno Nardelli, M. Calandra, R. Car, C. Cavazzoni, D. Ceresoli, M. Cococcioni, N. Colonna, I. Carnimeo, A. Dal Corso, S. de Gironcoli, P. Delugas, R. A. DiStasio, A. Ferretti, A. Floris, G. Fratesi, G. Fugallo, R. Gebauer, U. Gerstmann, F. Giustino, T. Gorni, J. Jia, M. Kawamura, H.-Y. Ko, A. Kokalj, E. Küçükbenli, M. Lazzeri, M. Marsili, N. Marzari, F. Mauri, N. L. Nguyen, H.-V. Nguyen, A. Otero-de-la-Roza, L. Paulatto, S. Poncé, D. Rocca, R. Sabatini, B. Santra, M. Schlipf, A. P. Seitsonen, A. Smogunov, I. Timrov, T. Thonhauser, P. Umari, N. Vast, X. Wu, and S. Baroni, J. Phys. Condens. Matter **29**, 465901 (2017).
[35] A. P. Kajdos and S. Stemmer, Appl. Phys. Lett. **105**, 191901 (2014).
[36] R. Engel-Herbert, Y. Hwang, and S. Stemmer, Appl. Phys. Lett. **97**, 062905 (2010).
[37] S. R. Provence, S. Thapa, R. Paudel, T. K. Truttmann, A. Prakash, B. Jalan, and R. B. Comes, Phys. Rev. Mater. **4**, 083807 (2020).
[38] S. Thapa, R. Paudel, M. D. Blanchet, P. T. Gemperline, and R. B. Comes, J. Mater. Res. **36**, 26 (2021).
[39] N. Fairley, V. Fernandez, M. Richard-Plouet, C. Guillot-Deudon, J. Walton, E. Smith, D. Flahaut, M. Greiner, M. Biesinger, S. Tougaard, D. Morgan, and J. Baltrusaitis, Appl. Surf. Sci. Adv. **5**, 100112 (2021).

[40]P. Xu, D. Phelan, J. Seok Jeong, K. Andre Mkhoyan, and B. Jalan, Appl. Phys. Lett. **104**, 082109 (2014).
[41]M. Acharya, E. Banyas, M. Ramesh, Y. Jiang, A. Fernandez, A. Dasgupta, H. Ling, B. Hanrahan, K. Persson, J. B. Neaton, and L. W. Martin, Adv. Mater. **34**, 2105967 (2022).
[42]Y. Wang, R. B. Comes, S. Kittiwatanakul, S. A. Wolf, and J. Lu, J. Vac. Sci. Technol. A **33**, 021516 (2015).
[43]C. Marini, O. Noked, I. Kantor, B. Joseph, O. Mathon, R. Shuker, B. J. Kennedy, S. Pascarelli, and E. Sterer, J. Phys. Condens. Matter **28**, 045401 (2016).